Predicting and Rationalizing the Soret Coefficient of Binary Lennard-Jones Mixtures in the Liquid State

Nils E. R. Zimmermann,* Gabriela Guevara-Carrion, Jadran Vrabec,* and Niels Hansen*

The thermodiffusion behavior of binary Lennard-Jones mixtures in the liquid state is investigated by combining the individual strengths of non-equilibrium molecular dynamics (NEMD) and equilibrium molecular dynamics (EMD) simulations. On the one hand, boundary-driven NEMD simulations are useful to quickly predict Soret coefficients because they are easy to set up and straightforward to analyze. However, careful interpolation is required because the mean temperature in the measurement region does not exactly reach the target temperature. On the other hand, EMD simulations attain the target temperature precisely and yield a multitude of properties that clarify the microscopic origins of Soret coefficient trends. An analysis of the Soret coefficient suggests a straightforward dependence on the thermodynamic properties, whereas its dependence on dynamic properties is far more complex. Furthermore, a limit of applicability of a popular theoretical model, which mainly relies on thermodynamic data, was identified by virtue of an uncertainty analysis in conjunction with efficient empirical Soret coefficient predictions, which rely on model parameters instead of simulation output. Finally, the present study underscores that a combination of predictive models and EMD and NEMD simulations is a powerful approach to shed light onto the thermodiffusion behavior of liquid mixtures.

1. Introduction

In the nineteenth century, Ludwig[1] and Soret[2] observed independently from each other that a temperature gradient in an isotropic mixture can induce a concentration gradient (**Figure 1**). This coupling phenomenon between heat and mass flow

N. E. R. Zimmermann, N. Hansen
Institute of Thermodynamics and Thermal Process Engineering
University of Stuttgart
Pfaffenwaldring 9, 70569 Stuttgart, Germany
E-mail: n.zimmermann@tuhh.de; niels.hansen@itt.uni-stuttgart.de
G. Guevara-Carrion, J. Vrabec
Thermodynamics and Process Engineering
Technische Universität Berlin
Ernst-Reuter-Platz 1, 10587 Berlin, Germany
E-mail: jadran.vrabec@upb.de

The ORCID identification number(s) for the author(s) of this article can be found under https://doi.org/10.1002/adts.202200311

is known as thermal diffusion, thermodiffusion, Ludwig–Soret effect, or simply Soret effect. Coupled heat and mass transfer occurs in many industrially relevant processes such as absorption, distillation, extraction, drying, crystallization, or condensation.[3] As a second-order effect, the mass flux induced by the Soret effect is usually relatively small, but it can play an important role in many natural[4,5] and technical processes.[6] Thermal diffusion can be employed to separate mixtures that are hard to handle by conventional methods,[3] for example, the fractionation of isomers,[7] isotopes,[8] polymers,[9] and colloids.[10] Further applications include surface coating,[11] geological carbon dioxide storage,[12] modeling of hydrocarbon reservoirs,[13] and hydrogen enriched flames.[6]

Chemical systems that undergo thermodiffusion in practical settings are frequently binary systems in the liquid state. In such cases, the separation of the two components can be quantified by the Soret coefficient S_T, which is a preferred quantity in the study of liquids.[14] In case of multicomponent mixtures, the Soret coefficient becomes a vectorial quantity.[15] The Soret coefficient relates the thermal diffusion coefficient D_T to the Fick diffusion coefficient D

$$S_T = \frac{D_T}{D} \tag{1}$$

From a technological perspective, the Soret coefficient provides a compact metric to rate the separation efficiency of a process that is based on thermodiffusion (Figure 1).

Two factors render the measurement of the Soret coefficient usually challenging: first, the small magnitude of S_T and, second, the presence of undesirable convective currents due to gravitation.[16,17] Despite efforts to produce benchmark data,[12,18–21] some even in microgravity environments,[22,23] the measurement of the Soret coefficient is still challenging, in particular, for liquid mixtures with more than two components.[16,24] Consequently, several theoretical models were proposed to predict the Soret coefficient,[25–27] which were thoroughly reviewed, for example, in refs. [16, 28]. However, even the most established models based on non-equilibrium thermodynamics[16] often fail when dealing with strongly interacting liquid mixtures.
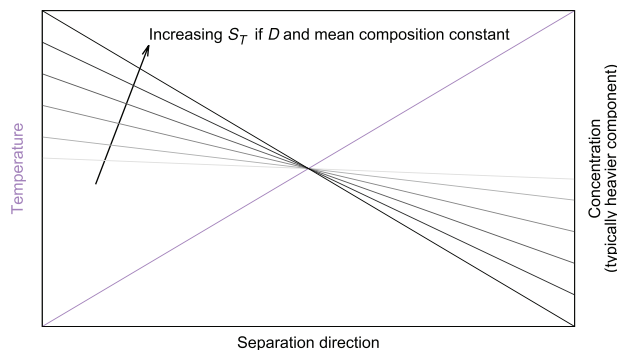
Molecular modeling and simulation offer a complimentary approach to gain a deeper understanding of the microscopic mech-

**ADVANCED
SCIENCE NEWS**

www.advancedsciencenews.com

**ADVANCED
THEORY AND
SIMULATIONS**

www.advtheorysimul.com

Figure 1. An increasing Soret coefficient S_T yields stronger separation of components if the temperature gradient, the Fick diffusion coefficient D, and the mean composition remain constant. The displayed behavior is referred to as positive thermodiffusion because the present component (typically the heavier one) accumulates in the low temperature region. By contrast, the component that accumulates in the high temperature region (typically the lighter one) undergoes negative thermodiffusion.

anisms of thermal diffusion and also allow for the prediction of Soret and other transport coefficients. The Lennard-Jones interaction potential is particularly attractive because it is a computationally efficient and yet realistic molecular model, thus helping to rapidly generate a fundamental understanding of molecular processes. Furthermore, Lennard-Jones mixtures can exhibit a rich vapor–liquid equilibrium behavior,[29–31] which can facilitate constructing new theoretical models and testing application limits of existing ones. Knowing the phase diagram is in itself central to studying thermodiffusion because phase changes are typically to be avoided, that is, gas bubbles and solid precipitates are unwanted when investigating thermal diffusion in the liquid state.

Thermodiffusion can be simulated in various ways by molecular simulations, where non-equilibrium molecular dynamics (NEMD) simulations are a well-established standard approach. These simulations closely mimic experimental scenarios for thermodiffusion measurements, making them the ideal candidates to construct benchmark data. NEMD simulations monitor the response to system perturbations out of equilibrium. Synthetic NEMD simulations[32–34] add external forces on molecules, thus altering their dynamics in an artificial way. On the contrary, boundary-driven NEMD methods[35–42] aim at paralleling experimental situations much more directly by their conceptual set-up. These methods impose different temperatures within the simulation volume that give rise to temperature gradients, which, in turn, exert thermodynamic forces on the molecules in an indirect and natural way. Typically, a narrow region along one spatial direction is assigned as a heat source volume, and a corresponding heat sink region is placed half the simulation volume apart. The difference between the various boundary-driven methods is the way in which the temperature is controlled in the two regions.

Another approach to simulate thermal diffusion and to calculate the Soret coefficient is based on the spontaneous fluctuations of the microscopic fluxes that are present in equilibrium molecular dynamics (EMD) simulations through the Green–Kubo formalism. Although the corresponding flux expressions for mixtures were thoroughly derived in the 1980s,[43,44] only a few molecular simulation studies on thermal diffusion employing EMD techniques can be found in the literature.[32,33,45–50] Further-

more, EMD methods have been mostly used for validation purposes, that is, together with NEMD simulations.[33,45–48,50] Presumably, this originates from the difficulties inherent to EMD simulations. First, cross-correlation functions are weaker and thus more challenging to sample than auto-correlation functions. Second, reliable information on the thermodynamic factor and the partial molar enthalpy is required to calculate the Soret coefficient. However, EMD simulations are valuable to gain insight into the sign and magnitude of the individual contributions to thermal diffusion processes, as recognized by Miller et al.[49]

In this work, the strengths of NEMD and EMD simulations were combined to reliably predict and understand the Soret coefficient of three different Lennard-Jones mixtures in the liquid state.[29,30] Furthermore, a popular theoretical model,[27] which mainly relies on thermodynamic input data, and a regression model to predict the Soret coefficient were tested, investigating their applicability limits. Our results and insights underscore that NEMD and EMD simulations in conjunction with theoretical models build a strong framework to foster understanding of thermodiffusion in liquid mixtures.

2. Methodology

When two or more processes occur simultaneously in a system, they may couple, causing new effects.[51] Examples of such cross-phenomena are the Soret and Dufour effects. The thermodiffusion or Soret effect addresses the macroscopic motion of molecules that results in a concentration gradient caused by a temperature gradient. The reciprocal phenomenon, that is, a temperature gradient caused by a concentration gradient, is known as Dufour effect.

2.1. Non-Equilibrium Thermodynamics

Linear non-equilibrium thermodynamics (NET) provides a compact framework to describe the behavior of systems subject to various driving forces and is fundamentally based on four postulates:[14]

1) the quasi-equilibrium postulate, requiring that gradients are not too large;
2) the linearity postulate, stating that all fluxes are linear functions of all relevant driving forces;
3) Curie's postulate, constraining which fluxes and forces are coupled; and
4) Onsager's reciprocal relations, requiring symmetric coefficient matrices in the flux-force relations.

Considering the Soret and Dufour effects only, the equations for heat flux $\mathbf{J}_Q$ and mass flux of component 1 $\mathbf{J}_1^m$ in a binary mixture can be written in the NET framework as[52]

$$\mathbf{J}_Q = -L_{QQ}\frac{\nabla T}{T^2} - L_{Q1}\left(\frac{\partial \mu_1}{\partial w_1}\right)_{T,p}\frac{\nabla w_1}{(1-w_1)T} \tag{2}$$

$$\mathbf{J}_1^m = -L_{1Q}\frac{\nabla T}{T^2} - L_{11}\left(\frac{\partial \mu_1}{\partial w_1}\right)_{T,p}\frac{\nabla w_1}{(1-w_1)T} \tag{3}$$

2200311 (2 of 13)

**ADVANCED
SCIENCE NEWS**

www.advancedsciencenews.com

**ADVANCED
THEORY AND
SIMULATIONS**

www.advtheorysimul.com

where T is the temperature, p is the pressure, and μ_1 and w_1 are the chemical potential and mass fraction of component 1, respectively. L_{ij} are phenomenological Onsager coefficients that describe the proportionality between the thermodynamic forces and the fluxes that they induce.[53] The auto-correlated properties L_{11} and L_{QQ} are the mass–mass and heat–heat phenomenological coefficients. The cross-correlated phenomenological coefficients $L_{1Q} = L_{Q1}$ follow Onsager's reciprocity relations.[54]

On the other hand, experimentalists usually employ the following constitutive equations[46,52] to describe heat and mass fluxes

$$\mathbf{J}_Q = -\lambda \nabla T - \rho_m w_1 \left(\frac{\partial \mu_1}{\partial w_1} \right)_{T,p} T D_T^D \nabla w_1 \qquad (4)$$

$$\mathbf{J}_1^m = -\rho_m w_1 w_2 D_T^S \nabla T - \rho D \nabla w_1 \qquad (5)$$

where λ is the thermal conductivity, ρ_m is the mass density of the mixture, and D_T^S and D_T^D represent the thermal diffusion coefficients of Soret- and Dufour-type, respectively.

When the steady state is reached (i.e., $\mathbf{J}_1^m = 0$) and a constant mass density can be assumed, Equation (5) can be rearranged to

$$S_T = \frac{D_T^S}{D} = -\frac{1}{w_1 w_2} \left(\frac{\nabla w_1}{\nabla T} \right)_{\mathbf{J}_1^m = 0} = -\frac{1}{x_1 x_2} \left(\frac{\nabla x_1}{\nabla T} \right)_{\mathbf{J}_1 = 0} \qquad (6)$$

where x_i is the mole fraction of component i and $\mathbf{J}_1$ the molar flux of component 1. Another frequently determined and closely related quantity is the thermal diffusion factor[52] α_T

$$\alpha_T = T S_T = T \frac{D_T}{D} \qquad (7)$$

The relations between phenomenological coefficients and transport coefficients can be determined by comparing the NET phenomenological Equations (2) and (3) with the constitutive Equations (4) and (5). Consequently, the thermal diffusion coefficients of Soret- and Dufour-type are thus given by[46]

$$D_T^S = \frac{L_{1Q}}{\rho_m w_1 w_2 T^2} \qquad (8)$$

$$D_T^D = \frac{L_{Q1}}{\rho_m w_1 w_2 T^2} \qquad (9)$$

From Onsager's reciprocity relations, it follows that $D_T^D = D_T^S = D_T$.

The Fick diffusion coefficient is related to the mass–mass phenomenological coefficient L_{11} by

$$D = L_{11} \frac{1}{\rho_m w_2 T} \left(\frac{\partial \mu_1}{\partial w_1} \right)_{T,p} = L_{11} \frac{k_B}{\rho w_1 w_2 M_1 M_2} \Gamma \qquad (10)$$

where ρ is the molar density of the mixture. M_i is the molar mass of component i, k_B is the Boltzmann constant, and Γ the thermodynamic factor. The Soret coefficient is thus[46]

$$S_T = \frac{1}{w_1 T} \frac{L_{1Q}}{L_{11}} \left(\frac{\partial w_1}{\partial \mu_1} \right)_{T,p} = \frac{w_1 M_2}{x_1 k_B T^2 \Gamma} \frac{L_{1Q}}{L_{11}} \qquad (11)$$
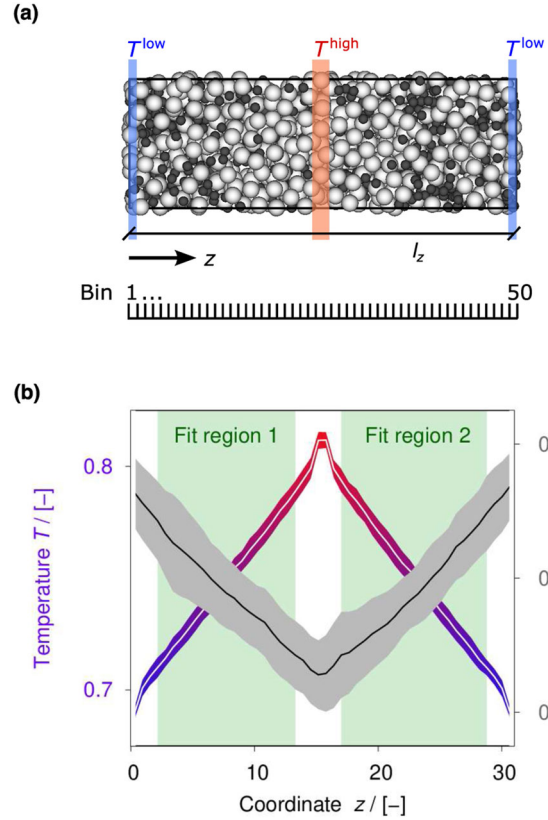
Figure 2. a) The key elements of the Langevin NEMD simulations are two temperature control regions. One of those regions (center) is maintained at a higher temperature T^{high}, whereas the outermost regions that are connected via periodic boundary conditions are kept at a lower temperature T^{low}. The temperature T and the mole fractions x_i as functions of the Cartesian z-direction are obtained from histograms using 50 bins. b) The profiles of T and x_1 obtained from Langevin NEMD simulations are linear. Two regions (green) can be used to determine slopes for further analysis to calculate the Soret coefficient.

2.2. Non-Equilibrium Molecular Dynamics

NEMD simulations closely mimic experimental scenarios to study thermodiffusion because these simulations exhibit regions of high and low temperature within the simulation volume. Furthermore, linear concentration profiles and linear temperature profiles in between these regions are obtained at steady state, the latter implying a constant thermal conductivity.[35] The thermal conductivity of pure Lennard-Jones fluids and binary mixtures increases with temperature and density,[35,55–57] the two effects possibly compensating each other. Thus, a narrow region in the center of the simulation volume is defined as a heat source and a corresponding region as a heat sink at the edges of the simulation volume in z-direction (**Figure 2**a).

The temperature profile $T(z)$ and the mole fraction profiles $x_i(z)$ were determined on the basis of particle trajectories obtained with LAMMPS[58] (stable version: October 29, 2020). Both temperature-control regions were of equal size, having a width of $0.3\sigma_1$, unless stated otherwise, where σ_1 is the Lennard-Jones size parameter of component 1. The resulting width was typically $\approx 1\%$ of the simulation volume. Two Langevin thermostats[59]

**ADVANCED
SCIENCE NEWS**

www.advancedsciencenews.com

**ADVANCED
THEORY AND
SIMULATIONS**

www.advtheorysimul.com

were used, where one thermostat heated one temperature-control region and the other thermostat cooled the other T-control region, so that we refer to this method as Langevin NEMD.

The Langevin NEMD simulations were typically carried out with 1200 molecules. The z-direction of the simulation volume was divided into 50 bins of constant width $\Delta z = l_z/50$ (Figure 2a). Each molecule i was assigned to one of the bins j, according to its position z_i: $j = \text{int}(z_i/\Delta z)$. For each bin j, the kinetic energy of all molecules located in the bin $E^{\text{kin}}(z_j)$ was determined

$$E^{\text{kin}}(z_j) = \frac{1}{2} \sum_{i=1}^{N(z_j)} m_i |\mathbf{v}_i - \mathbf{v}|^2 \tag{12}$$

where $N(z_j)$ is the number of molecules in bin j, m_i, and $\mathbf{v}_i$ the mass and the velocity of molecule i, respectively, and $\mathbf{v}$ is the center-of-mass velocity of the system. Since the total momentum of the system was set to zero, $\mathbf{v}$ vanishes. The local temperature in bin j $T(z_j)$ was calculated by[35]

$$T(z_j) = \frac{2 E^{\text{kin}}(z_j)}{3 N(z_j) k_B} \tag{13}$$

The number of degrees of freedom $3 N(z_j)$ should be adjusted to account for fixing the total momentum of the *entire* system, by subtracting three in total, but distributed over the entire temperature profile. Since 50 bins were typically used, we would need to subtract approximately $3/50 = 0.06$ from the number of degrees of freedom in each bin. As the number of degrees of freedom was typically $(3 \times 1200)/50 = 72$ in each bin with $N(z_j) \approx N/N_{\text{bins}} = 1200/50$, the adjustment would have been on the order of 0.1% and thus negligible. In this context, we investigated the influence of system size (i.e., the number of molecules) on the Soret coefficient—and thus on the temperature profile—while keeping the number of bins constant, and found no measurable influence when using larger systems, in agreement with previous work.[60] Usually, four different temperature differences ΔT between the region of high T^{high} and low temperature T^{low} were considered. The relative imposed temperature differences $(T^{\text{high}} - T^{\text{low}})/(0.5 \cdot (T^{\text{high}} + T^{\text{low}}))$ were set to 13.3%, 26.6%, 40%, and 53.3%, respectively. The largest temperature gradient observed in the simulations was 0.026 such that violation of local equilibrium is not expected.[61,62]

After a certain response time, a steady state was observed, where the temperature gradient induced a mole fraction gradient. The simulation time of 3500 to 5000 Lennard-Jones units spent to establish the steady state was selected based on transient density profiles reported by Bonella et al.[63] The mole fraction of component k in bin j $x_k(z_j)$ was calculated as the ratio of the number of molecules of component k in bin j $N_k(z_j)$ over the total number of molecules in bin j $N(z_j)$

$$x_k(z_j) = \frac{N_k(z_j)}{N(z_j)} \tag{14}$$

The slopes of the mole fraction dx_k/dz and temperature profiles dT/dz as well as the average mole fraction of component k $\bar{x}_k$ provide all required input data to calculate the Soret coefficient of component k using Equation (6). For each ΔT, ten simulations
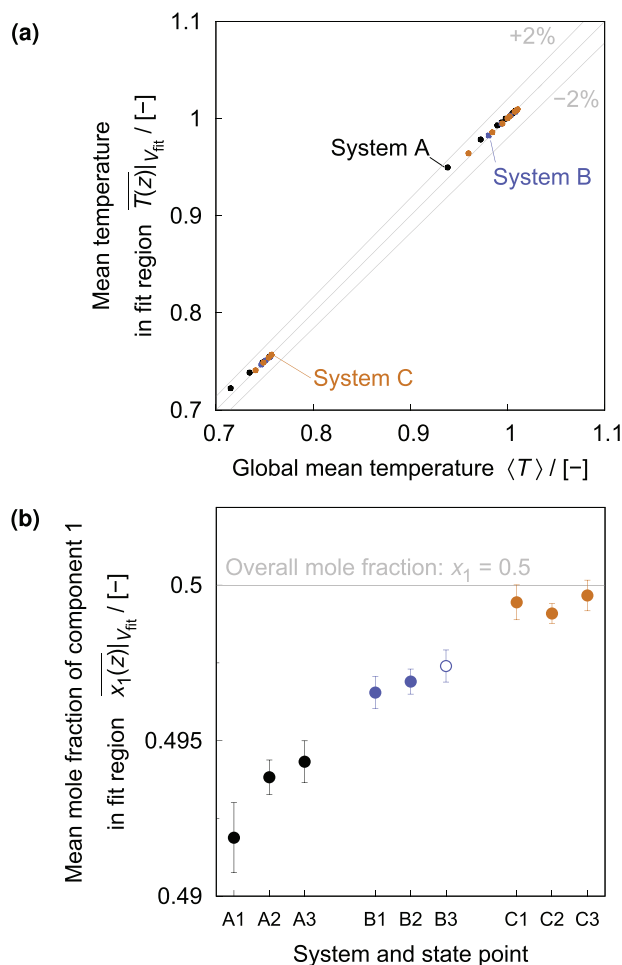
Figure 3. a) Parity plot of mean temperature in the profile fit region of the Langevin NEMD simulations $\overline{T(z)}|_{V_{\text{fit}}}$ and the global mean temperature $\langle T \rangle$ for all systems and state points studied in this work (cf. Table 1). b) Mean mole fraction of component 1 in the profile fit region of the Langevin NEMD simulations $\overline{x_1(z)}|_{V_{\text{fit}}}$ for all systems and state points.

with independent initial configurations were performed in order to average the individual Soret coefficient data and obtain reliable uncertainty estimates via the sample standard deviation.[64,65]

A transition regime was observed, in which the temperature and mole fraction profiles were still influenced by the temperature-control regions (Figure 2b). Therefore, all data points that were closer than $\approx 0.05 \times l_z$ to the center of each thermostat layer were discarded. Thus, roughly 20% of the profile data were discarded in order to maximize the likelihood to analyze linear profiles only.

Unless it is specified otherwise, the average temperature in the profile fit region V_{fit} was identified as the temperature of the NEMD simulations, that is, $T = \overline{T(z)}|_{V_{\text{fit}}}$. The average values from profiles agree very well with the corresponding global mean temperature obtained from *all* molecules in the *entire* NEMD simulation volume (**Figure 3**a). Similarly, the mean mole fraction of component 1 in the profile fit region of the NEMD simulations $\overline{x_1(z)}|_{V_{\text{fit}}}$ was close to the globally imposed value of $x_1 = 0.5$ mol mol^{-1} (Figure 3b).

**ADVANCED
SCIENCE NEWS**

www.advancedsciencenews.com

**ADVANCED
THEORY AND
SIMULATIONS**

www.advtheorysimul.com

Newton's equations of motion were integrated with a velocity-Verlet algorithm[66,67] during the production phase. More details about the NEMD simulations and the corresponding computational workflow are provided in Section S1.1, Supporting Information.

2.3. Equilibrium Molecular Dynamics

All EMD simulations were carried out with the *ms*2 package.[68] The mass–mass, heat–heat, and heat–mass phenomenological coefficients defined by the NET framework[52] can be sampled with EMD simulations, employing the Green–Kubo formalism.[69,70] In this framework, the phenomenological mass–mass phenomenological coefficient L_{11} is given by[44]

$$L_{11} = \frac{V}{3k_B} \int_0^\infty \langle \mathbf{J}_1^m(0)\mathbf{J}_1^m(t) \rangle \, dt \tag{15}$$

where t is the time. The microscopic mass flux $\mathbf{J}_i^m$ is defined as

$$\mathbf{J}_i^m(t) = \frac{1}{V} \sum_k^{N_i} m_i(\mathbf{v}_i^k(t) - \langle \mathbf{v} \rangle) \tag{16}$$

Here, m_i is the mass of a molecule of component i, $\mathbf{v}_i^k(t)$ the center of mass velocity vector of molecule k at some time t, N_i is the number of molecules of component i, and the angular brackets indicate the canonical (NVT) ensemble average. After setting the total momentum to zero, $\langle \mathbf{v} \rangle$ deviated from zero during simulation only within machine error such that $\mathbf{J}_1^m + \mathbf{J}_2^m = 0$.

The Green–Kubo expression for the heat–mass phenomenological coefficient L_{Q1} is

$$L_{Q1} = \frac{V}{3k_B} \int_0^\infty \langle \mathbf{J}_Q(t)\mathbf{J}_1^m(0) \rangle \, dt \tag{17}$$

In EMD simulations, the heat flux $\mathbf{J}_Q$ *cannot* be directly determined—in contrast to the internal energy flux $\mathbf{J}_E$ which *can* be directly computed. Thus, the associated internal energy–mass phenomenological coefficient L_{E1} was calculated by

$$L_{E1} = \frac{V}{3k_B} \int_0^\infty \langle \mathbf{J}_E(t)\mathbf{J}_1^m(0) \rangle \, dt \tag{18}$$

where the internal energy flux $\mathbf{J}_E$ is given by

$$\mathbf{J}_E = \frac{1}{2V} \sum_{i=1}^n \sum_{k=1}^{N_i} m_i^k (\mathbf{v}_i^k - \langle \mathbf{v} \rangle)^2 \cdot (\mathbf{v}_i^k - \langle \mathbf{v} \rangle)$$
$$- \frac{1}{2} \sum_{i=1}^n \sum_{j=1}^n \sum_{k=1}^{N_i} \sum_{l \neq k}^{N_j} \left[\mathbf{r}_{ij}^{kl} : \frac{\partial u_{ij}^{kl}}{\partial \mathbf{r}_{ij}^{kl}} - \mathbf{I} \cdot u_{ij}^{kl} \right] \cdot (\mathbf{v}_i^k - \langle \mathbf{v} \rangle) \tag{19}$$

Here, u_{ij}^{kl} is the inter-molecular potential energy and $\mathbf{r}_{ij}^{kl}$ is the distance vector between molecules k and l. The indices i and j denote the components of the mixture. The dyadic product is represented by : and $\mathbf{I}$ is the unitary tensor. In a binary mixture, L_{Q1}

can be determined from L_{E1} if the partial molar enthalpies h_i of both components are known[71]

$$L_{1Q} = L_{1E} - L_{11}\left(\frac{h_1}{M_1} - \frac{h_2}{M_2} \right) \tag{20}$$

Because of Onsager's reciprocity $L_{E1} = L_{1E}$. Thus, both cross-correlated coefficients were independently sampled during simulation and averaged to improve statistics.

2.3.1. Partial Molar Enthalpy

In this work, the partial molar enthalpy was calculated from EMD simulations in two steps. First, the residual molar enthalpy of the binary mixture h^{res} was calculated for ten different mole fractions in the isobaric–isothermal (NpT) ensemble over the composition range $x_1 = 0.5 \pm 0.05$ mol mol^{-1}. Subsequently, an appropriate function $h = f(x_1)$ was fitted by a least squares optimization to the simulation data to generate an expression for the molar enthalpy $h = h^{res} + h^{id}$.

The partial molar enthalpy h_i was then obtained from

$$h_i = h + x_j\left(\frac{\partial h}{\partial x_i} \right)_{T,p} \tag{21}$$

2.3.2. Thermodynamic Factor

To determine the Fick diffusion coefficient from the mass–mass phenomenological Onsager coefficients according to Equation (10), the thermodynamic factor Γ is required

$$\Gamma = \frac{x_1}{k_B T}\left(\frac{\partial \mu_1}{\partial x_1} \right)_{T,p} \tag{22}$$

It describes the thermodynamic non-ideality of a mixture and can be obtained from Kirkwood–Buff integrals[72] G_{ij}

$$G_{ij} = 4\pi \int_0^\infty (g_{ij}(r) - 1)r^2 \, dr \tag{23}$$

employing

$$\Gamma = 1 - \frac{\rho_1 \rho_2 (G_{11} + G_{22} - 2G_{12})}{\rho_1 + \rho_2 + \rho_1 \rho_2 (G_{11} + G_{22} - 2G_{12})} \tag{24}$$

where $g_{ij}(r)$ is the radial distribution function, while ρ_1 and ρ_2 are the partial densities $\rho_i = x_i \rho$. The truncation method by Krüger et al.[73] and the corrections of the radial distribution function by Ganguly and van der Vegt[74] were employed because of convergence issues.[75]

2200311 (5 of 13)

Table 1. Lennard-Jones parameters and state points.

System, state point	Mass ratio m_2/m_1	Size ratio σ_2/σ_1	Energy ratio $\varepsilon_2/\varepsilon_1$	Temperature $k_B T/\varepsilon_1$	Pressure $p\sigma_1^3/\varepsilon_1$	Cutoff radius r_{cut}/σ_1	Time step size $\Delta t/10^3$
A1	0.5	1.5	0.75	0.75	0.09	3.75	0.7071
A2	0.5	1.5	0.75	1	0.09	3.75	0.7071
A3	0.5	1.5	0.75	1	1.8	3.75	0.7071
B1	3.375	1.5	1	0.75	0.09	3.75	1
B2	3.375	1.5	1	1	0.09	3.75	1
B3	3.375	1.5	1	1	1.8	3.75	1
C1	1	1	0.75	0.75	0.09	2.5	1
C2	1	1	0.75	1	0.09	2.5	1
C3	1	1	0.75	1	1.8	2.5	1

2.4. Models

Equimolar (i.e., $x_1 = x_2 = 0.5$ mol mol^{-1}) binary liquid mixtures of molecules that interact via the Lennard-Jones potential were considered

$$u_{ij}^{kl} = 4 \cdot \varepsilon_{ij} \left[\left(\frac{\sigma_{ij}}{r_{ij}^{kl}} \right)^{12} - \left(\frac{\sigma_{ij}}{r_{ij}^{kl}} \right)^{6} \right] \tag{25}$$

where ε_{ij} and σ_{ij} are the Lennard-Jones energy and size parameter for the interaction between molecule pairs belonging to components i and j, and r_{ij}^{kl} denotes the distance between molecules k and l. The interaction parameters if $i = j$ σ_i and ε_i are provided in **Table 1**. The parameters for the interaction between different components were determined with the Lorentz–Berthelot combining rules[76] unless stated otherwise: $\sigma_{ij} = 0.5 (\sigma_i + \sigma_j)$ and $\varepsilon_{ij} = \sqrt{\varepsilon_i \varepsilon_j}$. Furthermore, the potential was explicitly evaluated up to a cutoff radius $r_{cut} = 2.5 \times \max(\sigma_1, \sigma_2)$,[39] and analytic tail corrections were applied to pressure and energy terms.[77,78] Small time step sizes Δt were chosen to integrate Newton's equations of motion[79] (Table 1).

All results are presented in Lennard-Jones units, where the mass m_1, the Lennard-Jones energy ε_1, and Lennard-Jones size parameters of component 1 σ_1 were used for reducing all quantities: $m^* = m/m_1$, $E^* = E/\varepsilon_1$, and $l^* = l/\sigma_1$, where E denotes energy and l length or distance. The reduced time and temperature are $t^* = t\sqrt{\varepsilon_1/(m_1\sigma_1^2)}$ and $T^* = Tk_B/\varepsilon_1$, respectively. For the sake of brevity, the asterisks on the reduced quantities are omitted in the remainder of this work.

3. Results

First, we present NEMD results because the corresponding Soret coefficients serve as a benchmark for the subsequent EMD simulations. For both approaches, specific issues, pitfalls, and necessary procedures are highlighted to obtain reliable Soret coefficient data. This is followed by a comparison and discussion of the data for all Lennard-Jones models considered in this work, where two lean prediction models are also included. The first model is based on thermodynamic and approximate kinetic data,[27]
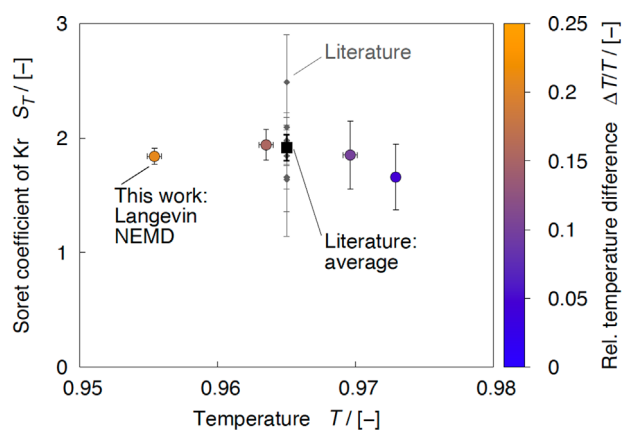

Figure 4. Soret coefficient of krypton S_T in its mixture with argon as a function of temperature T using the present Langevin NEMD method (circles). The color from blue to orange indicates an increasing relative temperature difference and thus a rising T gradient in the simulation volume. Literature values[32,33,35,41,49] (gray diamonds) and their average value[41] (black square) are provided for comparison.

whereas the second one is a regression model that relies on Lennard-Jones and mass parameters of the force field.[39]

3.1. NEMD: Creating a Benchmark

3.1.1. Validation

The Langevin NEMD method and the corresponding analysis workflow was validated on the basis of literature data for the mixture argon/krypton.[32,33,35,41,49] The present Soret coefficient data (**Figure 4**) agree well with data from literature, which were obtained using a broad variety of approaches: NEMD with synthetic NEMD simulations,[32,33] the heat exchange method,[35] as well as the modified heat exchange method and reverse NEMD simulations[41] and Green–Kubo-based EMD simulations.[49] The average temperature that was observed in the central profile-fit region of our simulation volume varied with the imposed temperature difference. The colors on the depicted data points correspond to the *observed* relative temperature difference $\Delta T/T$. It can be concluded that the present workflow is reliable but that it
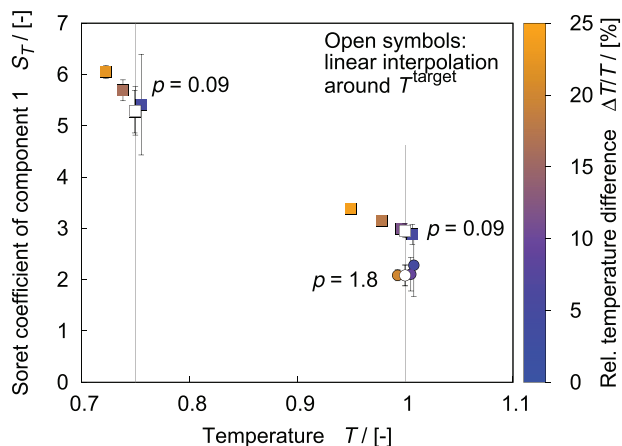
Figure 5. Soret coefficient of component 1 S_T for different temperatures T and target pressures p as obtained from Langevin NEMD simulations for the Lennard-Jones mixture A studied in this work (cf. Table 1). The color from blue to orange indicates an increasing relative temperature difference $\Delta T/T$ in the Langevin NEMD simulations. Open symbols represent linear interpolations of S_T and its standard deviation around the desired target temperature T^{target}. Corresponding plots for the other two Lennard-Jones mixtures are provided in the Supporting Information (Figure S5).

leaves some imprecision regarding the target temperature, which is on the order of 1%.

The Langevin NEMD procedure was also validated based on selected Lennard-Jones systems,[39,71] and the agreement was usually excellent (Figure S2, Supporting Information). Furthermore, the Langevin NEMD method and the enhanced heat exchange (eHEX) algorithm[40] as implemented in LAMMPS[58] yield consistent results (Figure S4, Supporting Information). Therefore, it can be concluded that the Langevin NEMD procedure reliably yields Soret coefficient data for Lennard-Jones systems.

3.1.2. Interpolation

The Soret coefficient from a given Langevin NEMD simulation is associated with the mean temperature in the fit region, which is the common practice when handling the rather complicated temperature-dependency of thermodiffusion quantities.[14] Typically, Soret coefficient data from NEMD simulations should be extrapolated to the zero-force regime,[32,39,80] where a linear function can be used.[39] However, MacGowan and Evans estimated zero-force transport coefficients by weighted averaging if a distinct force dependence of a given coefficient could not be detected.[32] On the one hand, the variation of the Soret coefficient is typically small for different thermodynamic driving forces around a given state point in this work (**Figure 5**). On the other hand, the average value of the temperature in the gradient fit region does not exactly match the target temperature (i.e., mean value of imposed high and imposed low temperature), but the deviations are small: a few percent. Furthermore, the Soret coefficient data determined with different gradients and at different temperatures usually exhibit consistent temperature trends (Figure 5). Therefore, comparison to EMD predictions, in which the target temperature is reached exactly, was facilitated by interpolation. Specifically, S_T and its standard deviation were linearly in-

terpolated in the small window around the target temperature to provide the most likely values at the target temperature.

3.1.3. Screening Other Influences

Validation on the basis of literature data and solving the interpolation issue were central to verifying the reliability of our Langevin NEMD method. However, other technical and model-related factors that can possibly influence the Soret coefficient were also sounded out. Specifically, it was reassured that the Langevin damping constant, the width of the temperature control regions, the system size, and the cutoff radius have no systematic impact on S_T (Section S2.4, Supporting Information), which leads us to the conclusion that the Langevin NEMD method proposed here yields reliable and robust results.
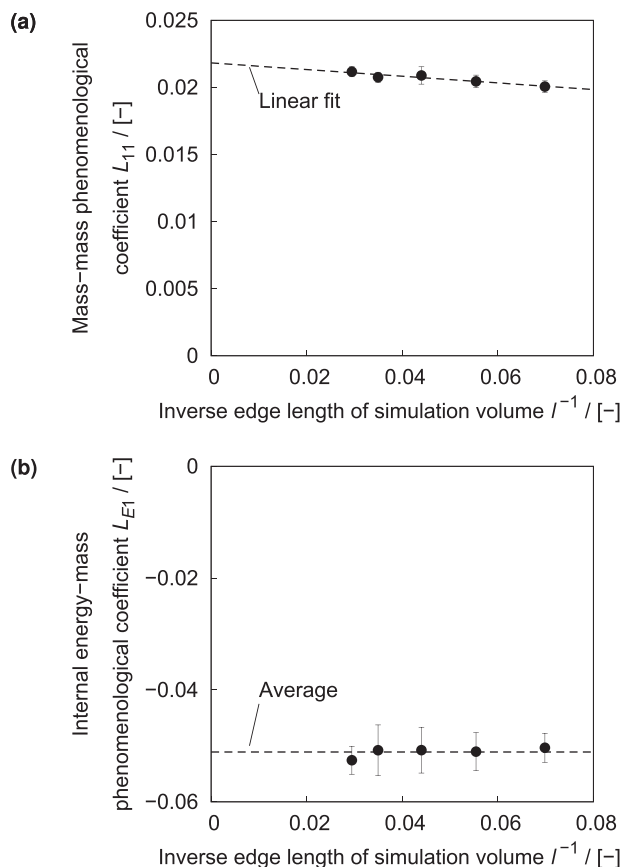
3.2. EMD: Obtaining Causal Data

The EMD approach based on correlation functions and the Green–Kubo formalism is challenging for dense liquids because the cross-correlations required to calculate thermal diffusion are at least one order of magnitude smaller than the auto-correlation functions[44] required to determine the self-diffusion coefficient. In a first step, EMD simulations were performed using the same simulation parameters as for the NEMD simulations (Table 1). The resulting Soret coefficient data are provided in Figure 8 and Table S1, Supporting Information. In a second step, the simulation parameters were optimized to yield consistent data with the NEMD simulations.

3.2.1. Finite Size Effects and Cutoff Radius

It is well known that small molecular systems under periodic boundary conditions are associated with systematic errors when diffusion coefficients are calculated. In this context, the size dependence of the mass–mass L_{11} and internal energy–mass L_{E1} phenomenological coefficients was studied for one of the considered systems (i.e., mixture B2). A series of simulations with varying system size containing 600, 1200, 2400, 4800, and 8000 molecules was performed. As expected, a clear system size dependence was observed for the mass–mass phenomenological coefficient L_{11} (**Figure 6**a). Its value in the thermodynamic limit, obtained by extrapolation to infinite size, was found to be 5.5% higher than its sampled value for 1200 molecules. Therefore, L_{11} had to be corrected to account for finite size effects when working with small systems, for example, as proposed in ref. [81]. A finite size correction of L_{11} based on a modified version of the correction factor by Yeh and Hummer [82,83] for binary mixtures yields an improvement, but L_{11} remains underestimated by 4%. On the other hand, no clear system size dependence could be inferred for the internal energy–mass coefficient L_{E1} despite its diffusive nature (Figure 6b).

The prediction of the thermodynamic factor by Kirkwood–Buff integration is also subject to system size effects, as can be seen in **Figure 7**. Because this formalism was originally derived for the grand canonical (μVT) ensemble, it has to be extrapolated to the

**ADVANCED
SCIENCE NEWS**

www.advancedsciencenews.com

**ADVANCED
THEORY AND
SIMULATIONS**

www.advtheorysimul.com

Figure 6. a) Mass–mass and b) internal energy–mass phenomenological coefficients of mixture B2 as functions of the inverse edge length of the simulation volume l^{-1}. The dashed lines are a linear fit and a fit of a constant (average) to the simulation results, respectively.

thermodynamic limit when the *NVT* ensemble is used. The correction method by Krüger et al.[73] was successfully employed in a previous work[75] to determine extrapolated values when dealing with small systems. However, when sufficiently large systems are employed, this methodology can lead to an over-correction of the thermodynamic factor (Figure 7).

Because of finite size-related issues, additional EMD simulations were performed with larger volumes for all studied mixtures. For this purpose, relatively large systems with 8000 molecules were employed and the cutoff radius was extended to half of the edge length of the simulation volume $l/2$. For mixture A2, the difference between the extrapolated and sampled mass transfer coefficient was within its statistical uncertainty (i.e., ≈ 2%). Further, the sampled thermodynamic factor differed by +2.5% from its extrapolated value. Therefore, the sampled values of the mass–mass phenomenological coefficient and the thermodynamic factor were employed directly without further finite size corrections for the calculation of the Soret coefficient. On the other hand, the coefficients sampled in a smaller simulation volume, containing 1200 molecules, do require finite size corrections.

Figure 8 shows the Soret coefficient of the studied Lennard-Jones mixtures for different system sizes (i.e., 1200 and 8000 molecules). As can be seen, there is a very good agreement be-
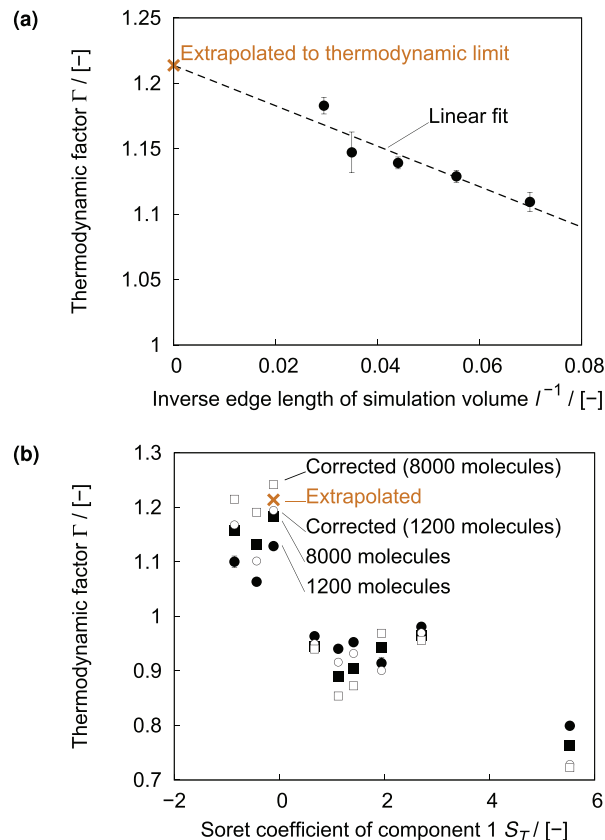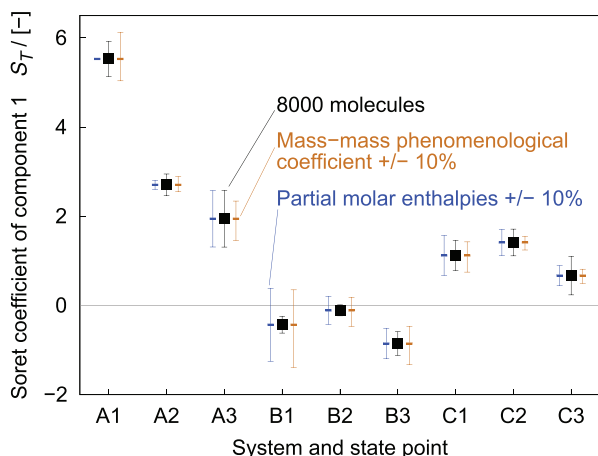

Figure 7. a) Thermodynamic factor of the mixture B2 as a function of the inverse edge length of the simulation volume l^{-1}, including a linear fit (dashed line) and the resulting extrapolated value in the thermodynamic limit (ochre cross). b) Thermodynamic factor sampled for systems with 1200 (solid circles) and 8000 (solid squares) molecules, respectively, and their corrected values (empty symbols) following Krüger et al.[73] as functions of the calculated Soret coefficient. The ochre cross represents the linearly extrapolated thermodynamic factor of mixture B2, as obtained from (a).
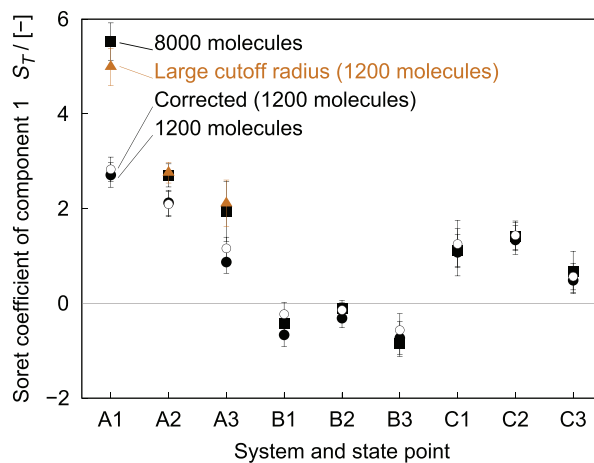
Figure 8. Soret coefficient calculated with 1200 (solid circles) and 8000 (solid squares) molecules. The open symbols represent coefficients calculated with the corrected mass–mass phenomenological coefficients[81] L_{11} and the corrected thermodynamic factor[73] Γ. The ochre symbols represent data calculated with 1200 molecules and a cutoff radius of $l/2$.

**ADVANCED
SCIENCE NEWS**

www.advancedsciencenews.com

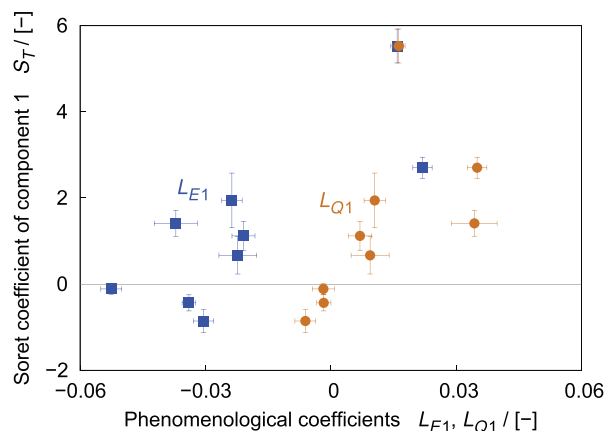**ADVANCED
THEORY AND
SIMULATIONS**

www.advtheorysimul.com

Figure 9. Range of the calculated Soret coefficient when the magnitude of the mass–mass phenomenological coefficient (ochre) changes by $\pm$ 10% and when the partial molar enthalpy difference $(h_1/M_1 - h_2/M_2)$ (blue) changes by $\pm$ 10%. The original Soret coefficient data with uncertainties (solid squares) were added for comparison.

Figure 10. Soret coefficient of component 1 as a function of the heat–mass phenomenological coefficient L_{Q1} and the internal energy–mass phenomenological coefficient L_{E1}, respectively, obtained from EMD simulations with 8000 molecules.

tween the Soret coefficient based on the simulations with 1200 molecules and those obtained from the simulations with 8000 molecules for the mixtures B and C. The peculiarly strong differences found for mixture A could be traced back to the use of a relatively short cutoff in the simulations with 1200 molecules. When the cutoff radius was changed to $l/2$, the agreement with the 8000 molecules simulation was significantly improved. A strong dependence of the cross-correlated phenomenological coefficient L_{E1} on the cutoff radius was found especially for mixture A1. Changes of other transport properties due to the cutoff radius (e.g., diffusion coefficients, shear viscosity, and thermal conductivity) were found to be within their statistical uncertainties. Negligible changes were also found for the thermodynamic equilibrium properties. Solely, the average pressure was 15% lower for the simulations with a smaller cutoff radius.

3.2.2. Sensitivity

Two factors were identified to highly affect the Soret coefficient value when predicted from EMD simulations: the mass–mass phenomenological coefficient and the difference between the partial molar enthalpies of both components $(h_1/M_1 - h_2/M_2)$. For the majority of considered mixtures, a change of a few percent of either of these quantities leads to a large change of the Soret coefficient. For example, **Figure 9** shows the resulting changes of the Soret coefficient when the mass–mass phenomenological coefficient L_{11} and the enthalpy difference $(h_1/M_1 - h_2/M_2)$ are varied by $\pm$10%. The strong variation of the Soret coefficient is related to L_{Q1}. As can be seen in **Figure 10**, the contribution of the enthalpy on the heat–mass phenomenological coefficient is large for most of the studied mixtures. Furthermore, in cases where terms of Equation (20) have a very similar magnitude a small change of the second term may even lead to a change of sign of the Soret coefficient.

Because of the strong sensitivity of the EMD simulations for the studied mixtures, the results obtained from the larger systems featuring 8000 molecules are regarded as the more ade-

quate values for comparison with NEMD results. The numerical results are listed in Table S2, Supporting Information.
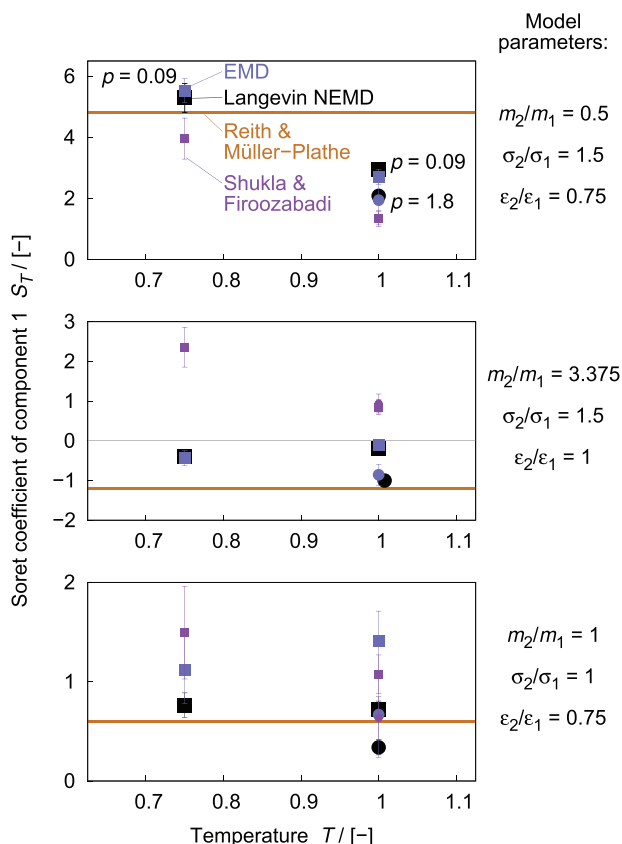
3.2.3. Other Properties

EMD simulations for the calculation of the Soret coefficient are challenging and have to be performed with carefully chosen parameters. However, all relevant quantities for gaining a microscopic understanding of the heat and mass transfer processes can be calculated directly with EMD: the Fick and the thermal diffusion coefficients as well as the thermal conductivity or the degree of coupling $q = L_{Q1}/(L_{11}L_{QQ})^{0.5}$. These quantities are listed in Table S3, Supporting Information.

3.3. NEMD versus EMD: Rationalizing S_T

Figure 11 shows the final data set with Soret coefficients of Lennard-Jones component 1 S_T from NEMD and EMD simulations as functions of temperature for two different average pressures and three Lennard-Jones mixtures (A, B and C; cf. Table 1). None of the systems studied gives rise to a sign change in the Soret coefficient and thus to a switch in thermophoretic behavior when the temperature or pressure is altered. The temperature and pressure ranges investigated are small and the data sparse. The observation is yet important because the change from positive to negative thermodiffusion behavior is subject of many studies due to the technological significance of this phenomenon.

The pressure impact on S_T is consistent across the different systems; however, the temperature influence can be different. In all cases, an increase in pressure from 0.09 to 1.8 yields a decrease of the Soret coefficient of component 1: by 30%, 417%, and 53% for mixtures A, B, and C, respectively. By contrast, S_T increases with rising temperature from 0.75 to 1 at $p = 0.09$ for mixture B by 50%, whereas it decreases by 44% and 6% for mixtures A and C, respectively. However, half of these relative change figures

$$d_{S_T} = 100 \times \frac{S_T(T_2 \text{ or } p_2) - S_T(T_1 \text{ or } p_1)}{|S_T(T_1 \text{ or } p_1)|} \% \tag{26}$$

**ADVANCED
SCIENCE NEWS**
www.advancedsciencenews.com

**ADVANCED
THEORY AND
SIMULATIONS**
www.advtheorysimul.com

Figure 11. Soret coefficient of component 1 S_T for different temperatures T and pressures p (squares: $p = 0.09$; circles: $p = 1.8$) of three different Lennard-Jones mixtures A (top), B (center), and C (bottom) as obtained from NEMD (black symbols) and EMD simulations (blue symbols). Theoretical predictions according to the model by Shukla and Firoozabadi[27] (small purple symbols) are also included as well as predictions on the basis of Reith's and Müller-Plathe's regression model (ochre solid line).[39]

exhibit large uncertainties when relying on a $2\sigma_{d_{S_T}}$ threshold to achieve 95% confidence. For the temperature-induced S_T changes, the uncertainties are 11%, 67%, and 37% and, for the pressure-induced S_T changes, they are 15%, 622%, and 23% for mixtures A, B, and C, respectively. We used the S_T uncertainties σ_{S_T} from the NEMD simulations to obtain the uncertainties $\sigma_{d_{S_T}}$ and applied conventional uncertainty propagation rules, which yields, for example, for the temperature-induced relative S_T change

mixture B, state point 2. The statistical uncertainties of S_T from EMD simulations are larger than those from NEMD simulations, which can be explained by the relatively small signal-to-noise ratio inherent to the cross-correlation functions. For mixtures A, all $1\sigma_{S_T}$ uncertainties are small, whereas those of mixtures B and C might seem moderate or large. This, however, is only a plotting effect because the vertical axis range in Figure 11 is more narrow for mixture B and much more narrow for mixture C.

3.4. Simulations versus Theoretical Models: Efficiently Predicting S_T

Several theoretical models[25,27,84,85] for predicting S_T leverage readily accessible thermodynamic information. In particular, the model by Shukla and Firoozabadi[27] is successful for gaseous and liquid mixtures.[86] The Soret coefficient is given by[27,86]

$$S_T^{\text{SF}} = -\frac{u_1/\tau_1 - u_2/\tau_2}{x_1(\partial\mu_1/\partial x_1)_{T,p}T} - \frac{(v_2 - v_1)(x_1 u_1/\tau_1 + x_2 u_2/\tau_2)}{(x_1 v_1 + x_2 v_2)x_1(\partial\mu_1/\partial x_1)_{T,p}T} \quad (28)$$

where u_i and v_i are the partial molar internal energy and the partial molar volume of component i, respectively. The component-specific factor τ_i, which is the cohesive energy of the liquid divided by the activation energy supplied for molecular motion,[27] ranges typically between three and five for liquids.[27,86] The predictions are included in Figure 11 using $\tau_i = 3.5$ (cf. ref. [86] and Section S2.6, Supporting Information). Since none of the state points chosen for the three considered Lennard-Jones mixtures is in the proximity of the critical point, the model should work well.[27]

We performed a detailed uncertainty propagation analysis[87] for the Soret coefficient given by the Shukla–Firoozabadi model (Section S2.6, Supporting Information). This could explain some of the discrepancies observed between NEMD, EMD, and predictive model results. For mixtures A and C, the model predicts the correct sign and most of the temperature and pressure dependences of S_T. The difference between NEMD simulation and model prediction relative to the model uncertainty is, on an average, however as large as 285% for these two mixtures. While uncertainties cannot be made fully responsible, they could contribute significantly to the deviations. In order to better understand the precise source of the model uncertainty, its relative contributions were calculated (Section S2.6 and Table S4, Supporting Information). The by-far largest contribution to the uncertainty in S_T^{SF} of component 1 stems from the τ_1 parameter σ_{τ_1}. The next largest contribution originates usually from σ_{τ_2}. The critical role

$$\sigma_{d_{S_T}} = 100 \times \left[\left(\frac{\sigma_{S_T(T_2)}}{|S_T(T_1)|} \right)^2 + \left(\frac{\sigma_{S_T(T_1)} \times [-|S_T(T_1)| - (\pm 1)(S_T(T_2) - S_T(T_1))]}{[S_T(T_1)]^2} \right)^2 \right]^{0.5} \% \quad (27)$$

where the factor ± 1 depends on whether $S_T(T_1) \gtrless 0$.

NEMD and EMD simulations usually yield consistent results because the $1\sigma_{S_T}$ uncertainties always overlap—with exception of

of the τ parameters is also reflected in the inability of the model by Shukla and Firoozabadi to predict the correct sign of S_T for highly asymmetric mixture B. Here, the regression model by Re-

**ADVANCED
SCIENCE NEWS**

www.advancedsciencenews.com

**ADVANCED
THEORY AND
SIMULATIONS**

www.advtheorysimul.com

ith and Müller-Plathe[39] might help shed light onto the reason for the prediction failure.

The Reith–Müller-Plathe model consists of three additive quadratic functions, each of which was separately fitted to a series of NEMD-derived Soret coefficients. In each series, a single model parameter of component 1, m_1, σ_1, or ϵ_1, was systematically varied so that the impact of one model parameter was encoded in one quadratic function. The resulting overall Soret coefficient, which was successfully validated on realistic systems such as isotopic argon–argon, argon–krypton, and xenon–methane, is given by[39]

$$S_T^{RMP} = -0.7 \left(\frac{m_1}{m_2}\right)^2 + 9.5 \left(\frac{m_1}{m_2}\right) - 8.8$$

$$+ 67.4 \left(\frac{\sigma_1}{\sigma_2}\right)^2 - 179.3 \left(\frac{\sigma_1}{\sigma_2}\right) + 111.9$$

$$+ 4.4 \left(\frac{\epsilon_1}{\epsilon_2}\right)^2 + 3.5 \left(\frac{\epsilon_1}{\epsilon_2}\right) - 7.9 \tag{29}$$

The applicability ranges for the different contributions are limited by originally fitting within $m_1/m_2 \leq 8$, $\sigma_1/\sigma_2 \leq 1.25$, and $\epsilon_1/\epsilon_2 \leq 1.75$. Moreover, the Soret coefficient is not given in Lennard-Jones units but in $(10^{-3} \mathrm{K}^{-1})$. Hence, S_T^{RMP} has to be adjusted to the present unit system.

The regression model by Reith and Müller-Plathe can reliably predict the sign of the Soret coefficient. Furthermore, the magnitude of S_T^{RMP} is reasonable, considering the fact that this prediction does not incorporate any temperature or pressure/density dependence. Another drawback of this model is the assumption that there are no coupling effects among the Lennard-Jones mass, size, and energy parameters. However, it has been found that such effects play a non-negligible role for the prediction of thermodiffusion of equimolar Lennard-Jones mixtures.[88]

The insight that was gained from these predictions is that mass and Lennard-Jones size parameter have opposing effects on the Soret coefficient. The lower mass of component 1 alone would result in negative thermodiffusion, whereas the smaller size parameter would trigger positive thermodiffusion. It thus depends on which effect is stronger and hence which type of model parameter ratio is larger. In the case of mixture B, the mass ratio ultimately dictates the negative sign. The τ parameters used in the model by Shukla and Firoozabadi[27] were originally determined for real systems, for which size and mass typically correlate. It is therefore possible that these parameters require a re-optimization if size and mass strongly diverge, as seems to hold for mixture B. Very recently, Hoang and Galliero [89] came to a similar conclusion on the lack of reliability of the Shukla–Firoozabadi model for the prediction of thermal diffusion factors for Lennard-Jones mixtures that are asymmetric in size and mass.

Finally, note that another possibility to describe the effects of mass, size, and energy parameter ratios on transport properties of Lennard-Jones mixtures is the van der Waals one-fluid model.[76,90] This model considers the mixture to be a hypothetical pseudo-compound that approximates its equilibrium and

transport properties. [91] However, this approach has significant limitations when dealing with strongly asymmetric mixtures [56,91] so that is not applied to the present systems.

4. Conclusion

We used Langevin NEMD alongside EMD simulations to investigate the Soret coefficient of binary Lennard-Jones mixtures. The Langevin NEMD simulations served as benchmarks because EMD predictions based on the Green–Kubo formalism are challenging due to a weak signal-to-noise ratio of the cross-correlation functions, the strong system-size dependence of the mass–mass phenomenological coefficient, and the uncertainties related to the calculation of the thermodynamic factor. Once optimal settings for the EMD simulations were determined, the data-set from the EMD simulations was successfully used to rationalize the behavior of the Soret coefficient. Furthermore, the EMD data were leveraged to test the applicability of a lean theoretical model,[27] which allows for predictions of the Soret coefficient mainly based on thermodynamic data.

We could identify a limitation of the theoretical model by Shukla and Firoozabadi.[27] Importantly, a detailed uncertainty analysis, which has, to the best of our knowledge, not been performed for the model yet, and complementing insights from a regression model,[39] which leverages model parameters of the mixture chosen, helped us pinpointing the probable reason. The theoretical model is unable to account for opposing effects of mass and size on the Soret coefficient. A parameter that is mainly kinetic in nature plays here a major role in dictating the sign of the Soret coefficient and thus in the applicability of the analytical model. More elaborate models such as those by Artola et al.[92] could be used instead, but this model requires, for example, more transport data.

Extending the combination of NEMD and EMD simulations to more complex systems is expected to provide insight into practical applications of thermodiffusion. The NEMD method was successfully applied to study aqueous alkali halide solutions[93] as well as to ternary[94,95] and quaternary[94] liquid mixtures of organic molecules. For both methods, the sampling of species with low concentration poses a challenge in these applications.

Supporting Information

Supporting Information is available from the Wiley Online Library or from the author.

Acknowledgements

Conflict of Interest

The authors declare no conflict of interest.

Data Availability Statement

The data that support the findings of this study are openly available in Data Repository of the University of Stuttgart (DaRUS) at https://doi.org/10.18419/darus-2996, reference number 0.

Keywords

[1] C. Ludwig, *Sitzungsber. Akad. Wiss. Wien, Math.-Naturwiss. Kl.* **1856**, *20*, 539.
[2] M. C. Soret, *Ann. Chim. Phys.* **1881**, *5*, 293.
[3] Y. Demirel, V. Gerbaud, in *Nonequilibrium Thermodynamics*, Elsevier, Amsterdam, Netherlands **2019**, pp. 337–379.
[4] D. Braun, A. Libchaber, *Phys. Biol.* **2004**, *1*, P1.
[5] I. Budin, R. J. Bruckner, J. W. Szostak, *J. Am. Chem. Soc.* **2009**, *131*, 9628.
[6] F. H. Vance, P. de Goey, J. A. van Oijen, *Combust. Flame* **2020**, *216*, 45.
[7] G. Greyling, H. Pasch, *Anal. Chem.* **2015**, *87*, 3011.
[8] F. Huang, P. Chakraborty, C. C. Lundstrom, C. Holmden, J. J. G. Glessner, S. W. Kieffer, C. E. Lesher, *Nature* **2010**, *464*, 396.
[9] A. Voit, A. Krekhov, W. Köhler, *Phys. Rev. E* **2007**, *76*, 011808.
[10] R. Piazza, A. Parola, *J. Phys.: Condens. Matter.* **2008**, *20*, 153102.
[11] H. Kania, J. Sipa, *Materials* **2019**, *12*, 1400.
[12] A. Mialdun, V. Shevtsova, *J. Chem. Phys.* **2011**, *134*, 044524.
[13] K. Ghorayeb, A. Firoozabadi, *SPE J.* **2000**, *5*, 158.
[14] R. B. Bird, W. E. Stewart, E. N. Lightfoot, *Transport Phenomena*, 2nd ed., John Wiley & Sons, Inc., New York **2007**.
[15] J. M. Ortiz de Zárate, *Eur. Phys. J. E: Soft Matter Biol. Phys.* **2019**, *42*, 43.
[16] M. Rahman, M. Saghir, *Int. J. Heat Mass Transfer* **2014**, *73*, 693.
[17] P. Costesèque, A. Mojtabi, J. K. Platten, *C. R. Méc.* **2011**, *339*, 275.
[18] J. K. Platten, M. M. Bou-Ali, J. F. Dutrieux, *Philos. Mag.* **2003**, *83*, 2001.
[19] G. Wittko, W. Köhler, *Philos. Mag.* **2003**, *83*, 1973.
[20] C. Leppla, S. Wiegand, *Philos. Mag.* **2003**, *83*, 1989.
[21] M. M. Bou-Ali, J. J. Valencia, J. A. Madariaga, C. Santamaría, O. Ecenarro, J. F. Dutrieux, *Philos. Mag.* **2003**, *83*, 2011.
[22] A. Vailati, R. Cerbino, S. Mazzoni, C. J. Takacs, D. S. Cannell, M. Giglio, *Nat. Commun.* **2011**, *2*, 290.
[23] V. Shevtsova, A. Mialdun, D. Melnikov, I. Ryzhkov, Y. Gaponenko, Z. Saghir, T. Lyubimova, J. C. Legros, *C. R. Méc.* **2011**, *339*, 310.
[24] W. Köhler, K. I. Morozov, *J. Non-Equilib. Thermodyn.* **2016**, *41*, 151.
[25] E. L. Dougherty, Jr, H. G. Drickamer, *J. Chem. Phys.* **1955**, *23*, 295.
[26] A. G. Guy, *Int. J. Thermophys.* **1986**, *7*, 563.
[27] K. Shukla, A. Firoozabadi, *Ind. Eng. Chem. Res.* **1998**, *37*, 3331.
[28] M. Eslamian, M. Z. Saghir, *J. Non-Equilib. Thermodyn.* **2009**, *34*, 2.
[29] V. I. Harismiadis, N. K. Koutras, D. P. Tassios, A. Z. Panagiotopoulos, *Fluid Phase Equilib.* **1991**, *65*, 1.
[30] J. Vrabec, A. Lotfi, J. Fischer, *Fluid Phase Equilib.* **1995**, *112*, 173.
[31] S. Stephan, H. Hasse, *Mol. Phys.* **2020**, *118*, e1699185.
[32] D. MacGowan, D. J. Evans, *Phys. Rev. A* **1986**, *34*, 2133.
[33] G. V. Paolini, G. Ciccotti, *Phys. Rev. A* **1987**, *35*, 5156.
[34] D. J. Evans, *Phys. Lett. A* **1982**, *91*, 457.
[35] B. Hafskjold, T. Ikeshoji, S. Kjelstrup Ratkje, *Mol. Phys.* **1993**, *80*, 1389.
[36] T. Ikeshoji, B. Hafskjold, *Mol. Phys.* **1994**, *81*, 251.
[37] F. Müller-Plathe, *J. Chem. Phys.* **1997**, *106*, 6082.
[38] F. Müller-Plathe, D. Reith, *Comput. Theor. Polym. Sci.* **1999**, *9*, 203.
[39] D. Reith, F. Müller-Plathe, *J. Chem. Phys.* **2000**, *112*, 2436.
[40] P. Wirnsberger, D. Frenkel, C. Dellago, *J. Chem. Phys.* **2015**, *143*, 124104.
[41] S. H. Mozaffari, S. Srinivasan, M. Z. Saghir, *J. Therm. Sci. Eng. Appl.* **2017**, *9*, 031011.
[42] C. Templeton, R. Elber, M. Ferrario, G. Ciccotti, *Mol. Phys.* **2021**, e1892849.
[43] R. Vogelsang, C. Hoheisel, G. V. Paolini, G. Ciccotti, *Phys. Rev. A* **1987**, *36*, 3964.
[44] C. Hoheisel, R. Vogelsang, *Comput. Phys. Rep.* **1988**, *8*, 1.
[45] S. Sarman, D. J. Evans, *Phys. Rev. A* **1992**, *45*, 2370.
[46] A. Perronace, G. Ciccotti, F. Leroy, A. H. Fuchs, B. Rousseau, *Phys. Rev. E* **2002**, *66*, 3.
[47] A. Perronace, C. Leppla, F. Leroy, B. Rousseau, S. Wiegand, *J. Chem. Phys.* **2002**, *116*, 3718.
[48] S. Yeganegi, M. Anbarfam, *J. Phys. Soc. Jpn.* **2007**, *76*, 044601.
[49] N. A. T. Miller, P. J. Daivis, I. K. Snook, B. D. Todd, *J. Chem. Phys.* **2013**, *139*, 144504.
[50] F. Bresme, J. Armstrong, *J. Chem. Phys.* **2014**, *140*, 016102.
[51] Y. Demirel, in *Nonequilibrium Thermodynamics* (Eds: Y. Demirel, V. Gerbaud), Elsevier, Amsterdam, **2002**, pp. 24–58.
[52] S. de Groot, P. Mazur, *Non-Equilibrium Thermodynamics*, Dover Publications, New York **1984**.
[53] P.-A. Artola, B. Rousseau, *Mol. Phys.* **2013**, *111*, 3394.
[54] K. A. Dill, S. Bromberg, *Molecular Driving Forces: Statistical Thermodynamics in Biology, Chemistry, Physics, and Nanoscience*, 2nd ed., Garland Science, Abingdon **2011**.
[55] S. Yeganegi, M. D. Ganji, *Chem. Phys.* **2005**, *318*, 171.
[56] M. Bugel, G. Galliéro, *Chem. Phys.* **2008**, *352*, 249.
[57] G. Galliéro, C. Boned, *Phys. Rev. E* **2009**, *80*, 061202.
[58] S. Plimpton, *J. Comput. Phys.* **1995**, *117*, 1.
[59] T. Schneider, E. Stoll, *Phys. Rev. B* **1978**, *17*, 1302.
[60] G. Galliéro, B. Duguay, J.-P. Caltagirone, F. Montel, *Fluid Phase Equilib.* **2003**, *208*, 171.
[61] B. Hafskjold, S. Kjelstrup Ratkje, *J. Stat. Phys.* **1995**, *78*, 463.
[62] S. Kjelstrup, D. Bedeaux, I. Inzoli, J.-M. Simon, *Energy* **2008**, *33*, 1185.
[63] S. Bonella, M. Ferrario, G. Ciccotti, *Langmuir* **2017**, *33*, 11281.
[64] P. I. Good, *Resampling Methods: A Practical Guide to Data Analysis*, 2nd ed., Birkhäuser, Boston **2001**.
[65] Math vault website, probability and statistics symbols, https://mathvault.ca/hub/higher-math/math-symbols/probability-statistics-symbols/ (accessed: August, **2021**).
[66] D. Frenkel, B. Smit, *Understanding Molecular Simulations—from Algorithms to Applications*, 2nd ed., Academic Press, San Diego **2002**.
[67] Lammps website, "run_style" command, https://docs.lammps.org/run_style.html (accessed: August **2021**).
[68] R. Fingerhut, G. Guevara-Carrion, I. Nitzke, D. Saric, J. Marx, K. Langenbach, S. Prokopev, D. Celný, M. Bernreuther, S. Stephan,

M. Kohns, H. Hasse, J. Vrabec, *Comput. Phys. Commun.* **2021**, *262*, 107860.

[69] M. S. Green, *J. Chem. Phys.* **1954**, *22*, 398.

[70] R. Kubo, *J. Phys. Soc. Jpn.* **1957**, *12*, 570.

[71] J. Armstrong, F. Bresme, *Phys. Chem. Chem. Phys.* **2014**, *16*, 12307.

[72] J. G. Kirkwood, F. P. Buff, *J. Chem. Phys.* **1951**, *19*, 774.

[73] P. Krüger, S. K. Schnell, D. Bedeaux, S. Kjelstrup, T. J. H. Vlugt, J.-M. Simon, *J. Phys. Chem. Lett.* **2013**, *4*, 235.

[74] P. Ganguly, N. F. A. van der Vegt, *J. Chem. Theory Comput.* **2013**, *9*, 1347.

[75] R. Fingerhut, J. Vrabec, *Fluid Phase Equilib.* **2019**, *485*, 270.

[76] J.-P. Hansen, I. R. McDonald, *Theory of Simple Liquids - with Applications to Soft Matter*, 4th ed., Academic Press, Oxford **2013**.

[77] Lammps website, "pair_modify" command, https://docs.lammps.org/pair_modify.html (accessed: June **2021**).

[78] H. Sun, *J. Phys. Chem. B* **1998**, *102*, 7338.

[79] F. Jensen, *Introduction to Computational Chemistry*, 2nd ed., John Wiley & Sons Ltd, West Sussex, England **2007**.

[80] P. T. Cummings, D. J. Evans, *Ind. Eng. Chem. Res.* **1992**, *31*, 1237.

[81] G. Guevara-Carrion, R. Fingerhut, J. Vrabec, *J. Phys. Chem. B* **2020**, *124*, 4527.

[82] I. C. Yeh, G. Hummer, *J. Phys. Chem. B* **2004**, *108*, 15873.

[83] S. H. Jamali, A. Bardow, T. J. H. Vlugt, O. A. Moultos, *J. Chem. Theory Comput.* **2020**, *16*, 3799.

[84] R. Haase, *Z. Phys.* **1950**, *127*, 1.

[85] L. J. T. M. Kempers, *J. Chem. Phys.* **2001**, *115*, 6330.

[86] P.-A. Artola, B. Rousseau, *Phys. Rev. Lett.* **2007**, *98*, 125901.

[87] H. H. Ku, *J. Res. Natl. Bur. Stand. (U. S.)* **1966**, *70C*, 263.

[88] G. Galliéro, *Fluid Phase Equilib.* **2004**, *224*, 13.

[89] H. Hoang, G. Galliéro, *Eur. Phys. J. E: Soft Matter Biol. Phys.* **2022**, *45*, 5.

[90] T. W. Leland, J. S. Rowlinson, G. A. Sather, *Trans. Faraday Soc.* **1968**, *64*, 1447.

[91] G. Galliéro, C. Boned, A. Baylaucq, F. Montel, *Fluid Phase Equilib.* **2006**, *245*, 20.

[92] P.-A. Artola, B. Rousseau, G. Galliéro, *J. Am. Chem. Soc.* **2008**, *130*, 10963.

[93] S. Di Lecce, F. Bresme, *Mol. Simul.* **2019**, *45*, 351.

[94] G. Galliéro, H. Bataller, J.-P. Bazile, J. Diaz, F. Croccolo, H. Hoang, R. Vermorel, P.-A. Artola, B. Rousseau, V. Vesovic, M. M. Bou-Ali, J. M. Ortiz de Zárate, S. Xu, K. Zhang, F. Montel, A. Verga, O. Minster, *npj Microgravity* **2017**, *3*, 20.

[95] S. H. Mozaffari, S. Srinivasan, M. Z. Saghir, *Can. J. Chem. Eng.* **2019**, *97*, 344.